

Chapter 2

Mathematical Modeling

The governing equations of the helicopter rotor blade enabling piezoceramic-axial, bending, and shear actuation are derived in this chapter and an outline of the aeroelastic analysis used in this book is given. A background on piezoelectric materials used in this book is also provided. Section 2.1 begins with an introduction to piezoelectric materials and Sect. 2.2 explains the piezoceramic actuation concept. Section 2.3 provides an introduction to terminology used in the helicopter field. In Sect. 2.4, structural modeling is explained. Section 2.5 explains the aerodynamic model used for the aeroelastic analysis. Section 2.6 presents the blade and hub loads. Section 2.7 explains the aeroelastic analysis of a rotor. Section 2.8 gives the summary of this chapter.

2.1 Piezoelectric Materials

Piezoelectricity stems from the Greek word *piezein*, meaning to press or squeeze. It was found out that quartz changed its dimensions when subjected to an electric field and conversely generated an electric charge when it was pressed. A piezoelectric material develops a potential across its boundaries when subjected to a mechanical stress (or pressure), and vice versa, when an electric field is applied to the material, a mechanical deformation ensues. Piezoelectric materials therefore fall in the class of smart materials which are typically controllable using some physical variable such as electric or magnetic fields or temperature. Ferroelectricity is a subgroup of piezoelectricity, where a spontaneous polarization exists that can be reoriented by application of an AC electric field. Two types of piezoceramics exist: Soft (Ex: PZT-5H, PZT-5A) and hard (Ex: PZT-4D, PZT-8).

Soft piezoceramics are donor-doped PZT (Lead zirconate titanate) and hard piezoceramics are considered to be acceptor-doped PZT's. Material research says that soft

Table 2.1 Differences between soft and hard piezoceramics

Property	Soft PZT	Hard PZT
Piezoelectric constants	Larger	Smaller
Permittivity	Higher	Lower
Electromechanical coupling factors	Higher	Lower
Resistance	High	Lower
Linearity	Poor	Better
Polarization/Depolarization	Easier	Difficult
Hysteresis	Greater	Lower

PZTs have an exceptionally high-domain wall mobility, while the hard piezoceramics suppress the domain wall response. Regions in the piezoceramic with uniformly oriented spontaneous polarization are called domains and the region between two such domains is called a domain wall. This characteristic leads to the following differences between soft and hard piezoceramics (Table 2.1).

When manufactured, a piezoelectric material has electric dipoles arranged in random directions. In order to avoid a random response from each of these dipoles, alignment of dipoles is required so that a uniform response is achieved when an external stimuli is applied as shown in Fig. 2.1. For poling (aligning), the material is heated above its Curie temperature and a strong electric field is applied. The direction in which the field is applied is the polarization direction, resulting in the alignment of the dipoles in that direction. For fixing the poling direction permanently, the material is cooled below its Curie temperature. Every piezoelectric material has a specific Curie temperature. Polarization never results into a full/perfect alignment of all dipoles to give the ideal piezoelectric effect; however, the polycrystalline ceramic exhibits a large piezoelectric effect. While the polarization is being carried out, the dipoles are properly aligned but as soon as the external stimuli are removed, there is an introduction of an extremely small amount of randomness in dipoles once again. This process is depicted in Fig. 2.2. During this process, there is a very small expansion of the material along the poling axis and a contraction in both

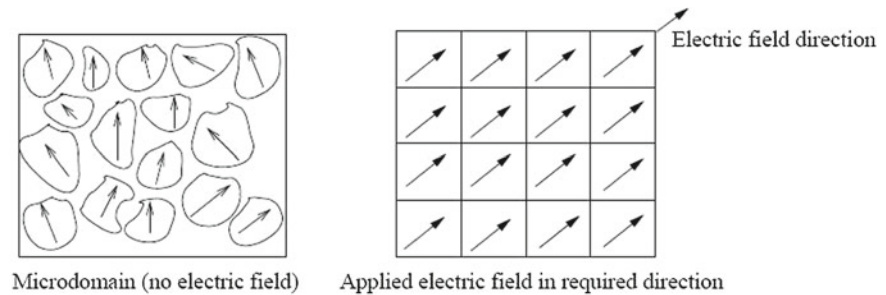


Fig. 2.1 Polarization in a piezoelectric domain

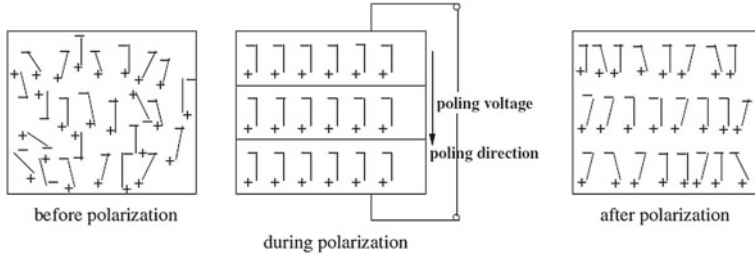


Fig. 2.2 Detailed polarization process

directions perpendicular to it. These dipoles after poling respond collectively to the external stimuli [1]. Application of an electric field (voltage) to a poled PZT results in its deformation (straining). Depolarization of the piezoelectric ceramic can result if it is exposed to excessive heat, electrical drive, or mechanical stress or any combination thereof. The temperature at which piezoelectric ceramic will be totally depoled is known as the “Curie point.” The constitutive equations are based on the assumption that the total strain is the sum of the mechanical strain induced by stress, the thermal strain induced by temperature, and the actuation strain dependent on applied electric field. The relation between strain and voltage is linear in the first order at relatively low electric fields and low mechanical stress levels. In general, piezoelectric materials are relatively linear at low electric fields and bipolar in nature. At high levels of electric fields, they exhibit nonlinearity to quite an extent. Although under an applied electric field they generate very low strains, they cover a wide range of actuation frequency [2].

Coupled electromechanical constitutive relations [3] for a piezoceramic are given as follows:

$$D_i = e_{ij}^\sigma E_j + d_{im}^d \sigma_m + a_i \Delta T \quad i = 1..3, \quad j = 1..3, \quad (2.1)$$

$$\epsilon_k = d_{jk}^c E_j + S_{km}^E \sigma_m + \alpha_{tk} \Delta T \quad k = 1..6, \quad m = 1..6. \quad (2.2)$$

Piezoelectric materials have the capability of undergoing strain on the application of an electric field. This concept is known as the converse piezoelectric effect (Eq. 2.2) and is exploited in actuators. Examples for the use of converse piezoelectric effect are sonar, ultrasound generation, positioners, motors, vibration cancellation, ultrasonic surgery, and so on. It allows the alteration of system characteristics as well as the system response. The same material (PZT) generates an electric charge when subjected to a mechanical force or deformation. This is known as the direct piezoelectric effect (Eq. 2.1) and is used in sensors. Examples for the use of direct piezoelectric effect are accelerometers, hydrophones, ultrasonic transducers, etc. The piezoelectric converse and direct effect is explained in Fig. 2.3. The microprocessors analyze the response from the sensors and use distributed parameter control theory to command the actuators to apply localized stresses to minimize the response of the system. Hence, piezoelectric materials are utilized either as actuators or sensors

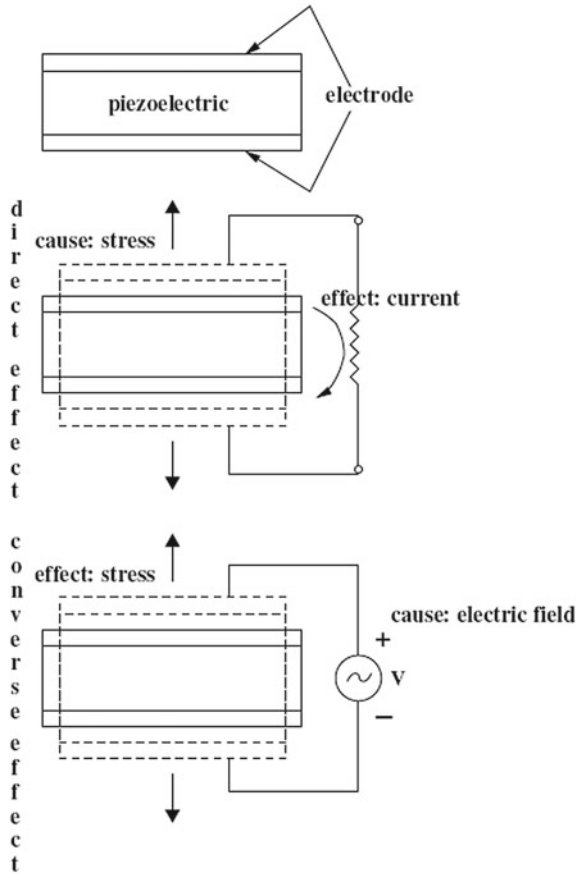
which ultimately contribute to a structure being smart. Since the structure can sense its environment and respond in a favorable manner, piezoelectric ceramic materials are typically employed as actuators (Eq. 2.2), while polymeric piezoelectric materials are typically employed as sensors (Eq. 2.1). Equation 2.2 could be rewritten in matrix form as follows:

$$\begin{Bmatrix} \epsilon_1 \\ \epsilon_2 \\ \epsilon_3 \\ \epsilon_{23} \\ \epsilon_{31} \\ \epsilon_{12} \end{Bmatrix} = \begin{bmatrix} S_{11} & S_{12} & S_{13} & 0 & 0 & 0 \\ S_{12} & S_{11} & S_{13} & 0 & 0 & 0 \\ S_{13} & S_{13} & S_{33} & 0 & 0 & 0 \\ 0 & 0 & 0 & S_{44} & 0 & 0 \\ 0 & 0 & 0 & 0 & S_{44} & 0 \\ 0 & 0 & 0 & 0 & 0 & S_{66} \end{bmatrix} \begin{Bmatrix} \sigma_1 \\ \sigma_2 \\ \sigma_3 \\ \tau_{23} \\ \tau_{31} \\ \tau_{12} \end{Bmatrix} \\
 + \begin{bmatrix} 0 & 0 & d_{31} \\ 0 & 0 & d_{32} \\ 0 & 0 & d_{33} \\ 0 & d_{15} & 0 \\ d_{15} & 0 & 0 \\ 0 & 0 & 0 \end{bmatrix} \begin{Bmatrix} E_1 \\ E_2 \\ E_3 \end{Bmatrix} + \begin{Bmatrix} \alpha_{tc1} \\ \alpha_{tc2} \\ \alpha_{tc3} \\ \alpha_{tc4} \\ \alpha_{tc5} \\ \alpha_{tc6} \end{Bmatrix} \Delta T. \quad (2.3)$$

Extension/Contraction in a piezoceramic element depends on the polarity of the electric field and the poling direction of the piezoceramic. The piezoceramic will shorten if a voltage of opposite polarity to the poling direction is applied to the electrode. If the applied voltage has same polarity as the poling voltage, the piezoceramic will lengthen. But if an AC voltage is applied to the electrodes, the piezoceramic will grow and shrink at the same frequency as that of the applied voltage. These phenomena are depicted in Fig. 2.4. Piezoelectric solid-state transducers are characterized by high forces in the range of kilo newtons, with reaction time of the order of a few milliseconds, along with a positioning accuracy of the order of a few nanometers. They have been successfully used over many years in a wide range of applications such as ultrasonic transducers, accelerometers, gramophones, resonators, filters, inkjet printers, and as various kinds of sensors in structural problems. Reviews on aerospace applications are given by [4]. Regarding the availability, there are various manufacturers who supply the characteristics of their products. Piezoelectrics are available in the form of sheets and films.

The advantages of piezoelectric materials being used as sensors and actuators include ease of integration into existing structures, easy control by voltage, low weight, low power requirements, low-field linearity, and high bandwidth (allowing large range of applications). In general, piezoelectric materials can be broadly classified into two groups: piezoceramics and piezopolymers. The most common piezoceramic is lead zirconate titanate (PZT) and the most common piezopolymer is Polyvinylidene Fluoride (PVDF). PZT is a ceramic and has high stiffness, while the PVDF polymer is more flexible and has low stiffness and high damping. The high stiffness of the PZT makes it a suitable actuator because of its high actuation authority and fast actuation response. In contrast, the flexibility and low stiffness of PVDF

Fig. 2.3 Direct and converse piezoelectric effect



makes it a better sensor. From these two types of piezoelectric material, there exist a variety of configurations in which they can be manufactured to be used as sensors and actuators. In terms of handling and practicality, the brittleness of piezoceramics places a restriction on its minimum thickness. Also, the attachment of piezoelectric materials to the host structure has to be performed with proper electrical insulation (Table 2.2).

2.1.1 Single Crystals

In general, relaxor-based ferroelectric single crystals have a different crystal composition and orientation as compared to conventional soft or hard piezoceramics. Physicists and metallurgists consider this structure to be very complex. Nonstoichiometric doping proved to be effective in creating instabilities in the material to

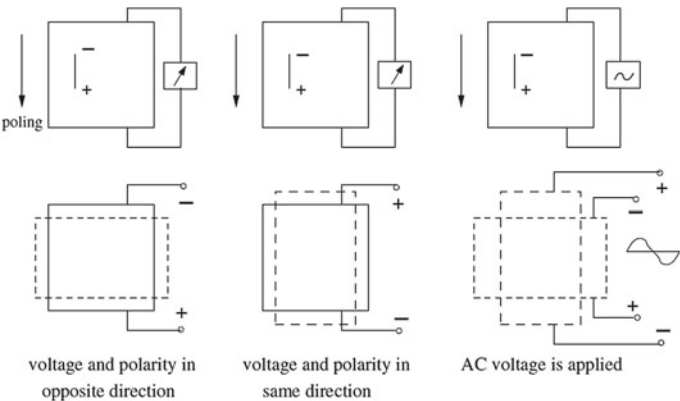


Fig. 2.4 Dependence of deformation on poling direction

Table 2.2 Nomenclature for the piezoceramic parameters

D = Dielectric displacement	(3×1) vector Newtons/milliVolts
e = Dielectric permittivity	(3×3) tensor Newtons/square Volt
E = Applied electric field	(3×1) vector Volts/meter
d = Piezoelectric coefficients	(3×1) vector meters/Volt
σ = Stress	(6×1) vector Newtons/square meter
a = Thermal constants	(6×1) vector Newtons/Volt-meter-degrees Kelvin
ΔT = Temperature	Constant degrees Kelvin
ϵ = Strain	(6×1) vector
S = Elastic compliance	(6×6) matrix square meters/Newton
α_{tc} = Thermal coefficient	(6×1) vector 1/degrees Kelvin

generate large responses, making the material “smarter.” The lead zirconate–lead titanate solid solution (PZT) system is one such successful example. The use of Nb doping can dramatically increase the value of the piezoelectric property of PZT. Of this category are $(1 - x)Pb(Zn_{1/3}Nb_{2/3})O_3 - xPbTiO_3$ (PZN–PT), and lead zinc niobate–lead titanate crystals. Here x is the percentage of $PbTiO_3$ in the crystal.

Domain engineered single-crystal systems (like PZN–PT) exhibit superior electro-mechanical properties compared to the conventional PZT ceramics. It is natural to ask the question, “Why the electromechanical properties have such values?” The answer to this lies in the crystallographic orientation and phase of the structure. It has been found that near the morphotropic phase boundary (MPB) between the rhombohedral and tetragonal phases, the levels of strain and the piezoelectric coefficients rise anomalously. In summary, without going into greater detail regarding the material configuration, this is the key to the high piezoelectric coefficients in single crystals like PZN–8 %PT.

Table 2.3 Comparison of the electromechanical properties

	Max strain %	Elastic energy density J/cm ³	Coupling efficiency (k^2) %	Relative speed full cycle
PZT	0.2	0.10	52	Fast
PZN-PT	1–1.7	1.0	81	Fast

Single-crystal materials are grown in crucibles at high, very tightly controlled temperatures using a starting seed to determine the crystallographic orientation. Orientations can be tailored to optimize response to longitudinal, transverse, and shear excitations commonly used in transducer designs. A significant reorientation of domains is achieved during polarization of single-crystal materials, resulting in higher electromechanical coupling factors (applied electrical energy is converted into mechanical or acoustic energy) of 90 % or more, as compared to 70 % for polarized conventional piezoceramics. Single-crystal piezoelectric materials also offer higher bandwidths, up to 135 %, as compared to 40–45 % for PZT. In actuator applications, single-crystal materials can achieve field-induced strains three times greater than those obtained in PZT. The dielectric losses in single crystal are much less than 1 %, as compared to 2 % for PZT. A quantitative comparison of the properties for general PZT and PZN-PT ceramics is made in Table 2.3 [5].

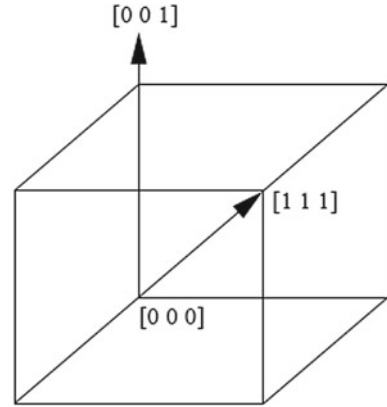
According to Park and Shrout [5], in designing an actuator, the maximum strain energy density should be as high as possible. Generally, the induced strain due to the applied field is the most important parameter for an actuators performance. This is also reflected in the strain energy density function which can be defined as below:

$$e_{max} = \frac{1}{\rho} \left(\frac{1}{4} \right) \left(\frac{1}{2} \right) E (s_{max}^2), \quad (2.4)$$

where e_{max} is the strain energy density, E is the actuators elastic modulus, s_{max} is the maximum field-induced strain, and ρ is the actuators density. The factor $1/4$ in Eq. 2.4 is appropriate for an actuator impedance related to its surroundings.

Piezoelectric properties of PZN-PT-type single crystals with $\langle 001 \rangle$ -orientation have been found to posses large direct piezoelectric coefficients (d_{33} , d_{31}) which are almost of the order of 10–15 times that of a soft piezoceramic such as PZT-5H. However, the shear coefficient d_{15} of these materials is relatively poor as compared to soft piezoceramics such as PZT-5H. Liu et al. [6] reported that the piezoelectric shear coefficient d_{15} of PZN-4.5 %PT and PZN-8 %PT crystals oriented in $\langle 111 \rangle$ is very high as compared to the conventional soft piezoceramic materials. Here, $\langle 001 \rangle$ and $\langle 111 \rangle$ orientations are directions in a crystal. These directions are shown in Fig. 2.5. Such single crystals are now commercially available and should therefore be evaluated for applications.

Fig. 2.5 The $\langle 001 \rangle$ and $\langle 111 \rangle$ orientations in a crystal

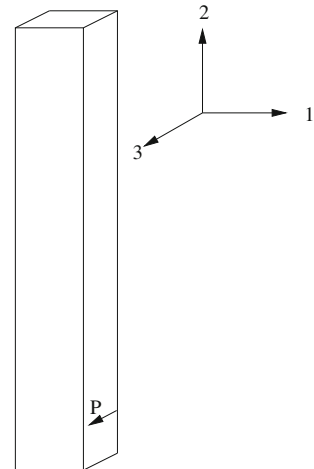


2.2 Piezoceramic Actuation

The relationship between induced strain and the applied electric field for piezoelectric materials can be understood with help of the piezoelectric constitutive equations. Modeling of induced strain actuation was addressed initially by Crawley [7] and later was discussed and validated in detail by Hong and Chopra [8]. The constitutive equations for piezoelectric material are ‘poling-direction’ dependent; therefore, appropriate care should be taken when using them. For a piezoelectric segment, there are three directions in which poling can be established.

- If axial and bending actuation is desired, poling direction should be selected as ‘3.’ For a piezo segment shown in Fig. 2.6, poling is in the 3 direction and the constitutive equations can be written as

Fig. 2.6 Configuration of a piezo segment with poling direction 3



$$\begin{Bmatrix} \lambda_{11} \\ \lambda_{22} \\ \lambda_{33} \\ \lambda_{23} \\ \lambda_{31} \\ \lambda_{12} \end{Bmatrix} = \begin{bmatrix} 0 & 0 & d_{31} \\ 0 & 0 & d_{32} \\ 0 & 0 & d_{33} \\ 0 & d_{24} & 0 \\ d_{15} & 0 & 0 \\ 0 & 0 & 0 \end{bmatrix} \begin{Bmatrix} E_1 \\ E_2 \\ E_3 \end{Bmatrix}. \quad (2.5)$$

This relationship is found in most literature where poling in 3 direction is assumed. Here, λ is the actuation strain and in general, the first subscript of the d-constant d_{jk} gives the “electrical” direction (field or dielectric displacement) and the second gives the component of mechanical deformation or stress. The convention is to define the poling direction as the 3-axis, and the shear planes are indicated by the subscripts 4, 5, and 6 and are perpendicular to directions 1, 2, and 3, respectively. The planar isotropy of poled ceramics is expressed in their piezoelectric constants by the equalities $d_{32} = d_{31}$ (an electric field parallel to the poling axis 3 interacts in the same way with axial stress along either the 2-axis or the 1-axis) and $d_{24} = d_{15}$. Similar relations hold for the elastic constants because of the isotropy in the plane perpendicular to the polar axis. In general, the piezoelectric strain coefficients d_{15} and d_{24} contribute to shear strains and others to normal strains.

- If shear/torsional actuation is desired, then the poling direction should be selected in the length direction, which is ‘2’ as shown in Fig. 2.7. For such a piezo segment, the constitutive equations can be written as

$$\begin{Bmatrix} \lambda_{11} \\ \lambda_{22} \\ \lambda_{33} \\ \lambda_{23} \\ \lambda_{31} \\ \lambda_{12} \end{Bmatrix} = \begin{bmatrix} 0 & d_{31} & 0 \\ 0 & d_{33} & 0 \\ 0 & d_{32} & 0 \\ 0 & 0 & d_{24} \\ 0 & 0 & 0 \\ d_{15} & 0 & 0 \end{bmatrix} \begin{Bmatrix} E_1 \\ E_2 \\ E_3 \end{Bmatrix}. \quad (2.6)$$

Fig. 2.7 Configuration of a piezo segment with poling direction 2

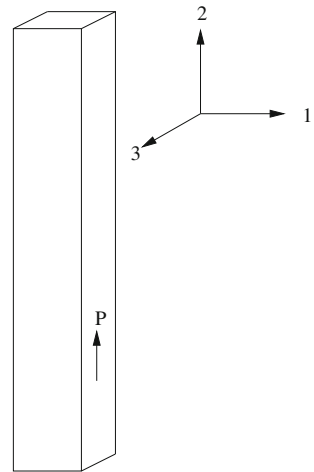
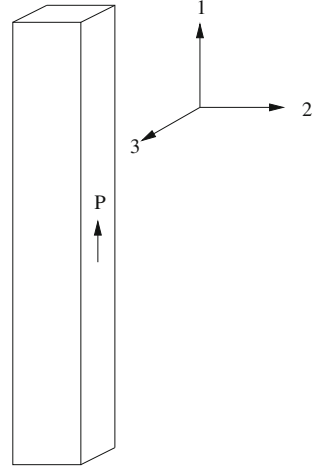


Fig. 2.8 Configuration of a piezo segment with poling direction 1



One can select the case which corresponds to the poling in the span/length direction. But the coordinate system that we refer to is different from that mentioned in the above cases. Thus, we transform case 2 to the following coordinate system

$$\begin{Bmatrix} \lambda_{11} \\ \lambda_{22} \\ \lambda_{33} \\ \lambda_{23} \\ \lambda_{31} \\ \lambda_{12} \end{Bmatrix} = \begin{bmatrix} d_{33} & 0 & 0 \\ d_{31} & 0 & 0 \\ d_{32} & 0 & 0 \\ 0 & 0 & 0 \\ 0 & 0 & d_{24} \\ 0 & d_{15} & 0 \end{bmatrix} \begin{Bmatrix} E_1 \\ E_2 \\ E_3 \end{Bmatrix}. \quad (2.7)$$

For the piezoelectric segment shown in Fig. 2.8, the span and poling direction is the '1' direction. It can be seen from Eq. 2.7 that both λ_{31} and λ_{12} utilize d_{15} . In Chaps. 8–11 of this book, the shear strain λ_{12} is employed to produce twist in the structure.

2.3 Key Terminologies and Nondimensional Parameters

Since this book deals with helicopter main rotor, some key terminologies used in this book are explained first. Figure 2.9 shows the rotor disk. Any point on the rotor disk can be located based on the polar coordinates (r, ψ) . Here, r is the radial location and varies from $r = 0$ at the hub to $r = R$ at the tip, where R is the blade radius. The rotor rotates counterclockwise with a constant rotation speed of Ω and moves forward with a speed of V . When the blade is at $\psi = 90^\circ$, it is at the advancing side of the rotor. When the blade is at $\psi = 270^\circ$, it is at the retreating side of the rotor.

Fig. 2.9 Rotor disk of the helicopter

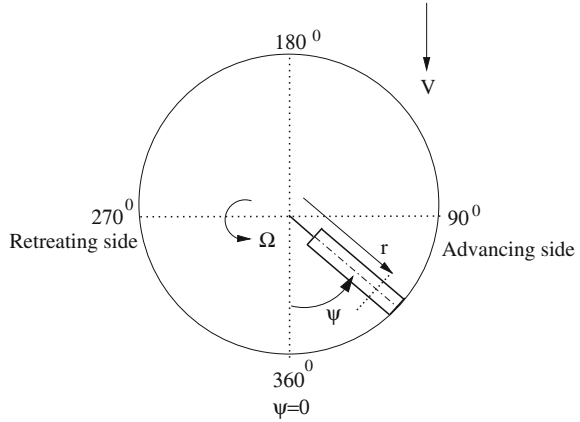
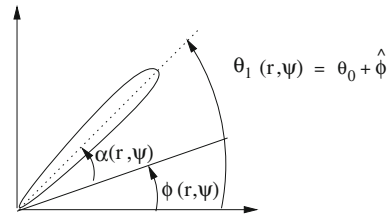


Fig. 2.10 Blade cross section



At any section (r, ψ) , the blade section is an airfoil as shown in Fig. 2.10. The angle of attack at any blade section can be written as

$$\alpha(r, \psi) = \theta_1(r, \psi) - \phi(r, \psi), \quad (2.8)$$

where $\theta_1(r, \psi)$ is the local blade pitch and $\phi(r, \psi)$ is the local inflow angle. The inflow angle is usually obtained from a wake model. Wake models for helicopters range from momentum theory which assumes a uniform inflow to free wake models which account for the nonuniformity in inflow which is characteristic of real rotors. Blade section loads are calculated using the angle of attack, $\alpha(r, \psi)$. The local blade pitch $\theta_1(r, \psi)$ includes the effect of both pilot control input θ_0 and elastic twist $\hat{\phi}$.

The nondimensional forward speed (μ), thrust coefficient (C_T), power coefficient (C_P), lock number, and solidity of a rotor are defined below. Here, μ is defined as the ratio of the forward speed of the helicopter to the rotor tip rotation speed (ΩR). Lock number γ is defined as the ratio of aerodynamic forces to the inertial forces and solidity (σ) is defined as the ratio of rotor blade area to rotor disk area.

$$\begin{aligned}
\mu &= \frac{V}{\Omega R}, \\
C_T &= \frac{T}{\frac{1}{2} \rho A (\Omega R)^2}, \\
C_P &= \frac{P}{\frac{1}{2} \rho A (\Omega R)^3}, \\
\gamma &= \frac{\rho C_{l\alpha} c R^4}{I_b}, \\
\sigma &= \frac{N_b c}{\pi R}.
\end{aligned}$$

Here, V is the forward speed of the helicopter, ρ is the density of air, Ω is the rotor rotational speed, T is the thrust, P is the power, $C_{l\alpha}$ is the lift curve slope, c is the blade chord, and I_b is the mass moment of inertia about the flapping hinge. Also, A is the rotor disk area and N_b is the number of blades.

2.3.1 Nondimensionalization

The entire formulation and all computations are carried out in nondimensional form. In addition to increase the generality of the analysis, working with nondimensional quantities can help avoid scaling problems while computing. It should be noted that the following physical quantities are nondimensionalized by the given reference parameters. Only nondimensional quantities are used in the analysis (Table 2.4).

Here, m_0 is defined as the reference mass per unit length of an equivalent uniform blade which has the same flap inertia as the actual (nonuniform) blade. Using this definition, m_0 can be defined as follows:

$$m_0 = \frac{3 \int_0^R m r^2 dr}{R^3}. \quad (2.9)$$

Table 2.4 Nondimensionalization

Physical quantity	Reference parameter
Length	R
Time	$1/\Omega$
Mass/length	m_0
Velocity	ΩR
Acceleration	$\Omega^2 R$
Force	$m_0 \Omega^2 R^2$
Moment	$m_0 \Omega^2 R^3$
Energy or work	$m_0 \Omega^2 R^3$

2.4 Structural Modeling

2.4.1 Hamilton's Principle

The generic governing differential equations are derived for a smart beam/rotor blade undergoing axial, chord-wise bending, span-wise bending and elastic twist and supporting axial, bending, and torsion actuation. A point P on the undeformed elastic axis undergoes deflection u, v, w in the x, y, z and moves to a point P' as shown in Fig. 2.11. X and Y are the hub coordinate axes and blade is at a precone angle β_p from the hub axes. The cross section undergoes a rotation θ_1 as shown in Fig. 2.12. Here θ_0 is given as

$$\theta_0 = \theta_{75} + \theta_{tw} \left(\frac{x}{R} - 0.75 \right) + \theta_{1c} \cos \psi + \theta_{1s} \sin \psi, \quad (2.10)$$

where θ_{75} is the blade pitch at 75 % span of blade, θ_{tw} is the blade linear pretwist, and θ_{1s} and θ_{1c} are the cyclic pitch controls.

The constitutive equations of an isotropic beam plate [9] can be written as follows:

$$\begin{Bmatrix} \epsilon_{xx} \\ \epsilon_{\eta\eta} \\ \epsilon_{\zeta\zeta} \\ \epsilon_{x\eta} \\ \epsilon_{\eta\zeta} \\ \epsilon_{x\zeta} \end{Bmatrix} = \begin{bmatrix} 1/E & -\nu/E & -\nu/E & 0 & 0 & 0 \\ -\nu/E & 1/E & -\nu/E & 0 & 0 & 0 \\ -\nu/E & -\nu/E & 1/E & 0 & 0 & 0 \\ 0 & 0 & 0 & 1/G & 0 & 0 \\ 0 & 0 & 0 & 0 & 1/G & 0 \\ 0 & 0 & 0 & 0 & 0 & 1/G \end{bmatrix} \begin{Bmatrix} \sigma_{xx} \\ \sigma_{\eta\eta} \\ \sigma_{\zeta\zeta} \\ \tau_{x\eta} \\ \tau_{\eta\zeta} \\ \tau_{x\zeta} \end{Bmatrix}. \quad (2.11)$$

The following fundamental assumptions are made for the analysis [10]:

- (i) Mid-line of a plate segment does not deform in its own plane;
- (ii) the normal stress in the contour direction, $\sigma_{\eta\eta}$, is neglected relative to the normal axial stress σ_{xx} ; and

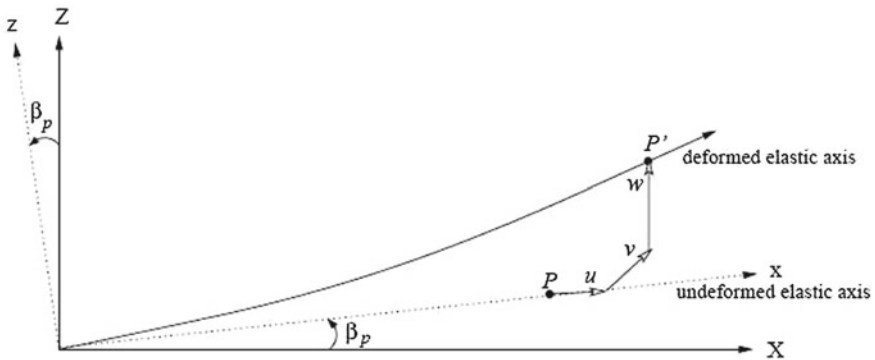
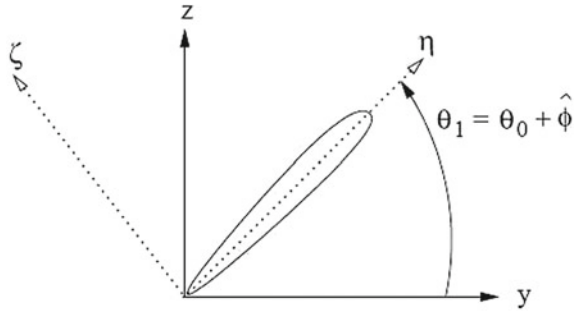


Fig. 2.11 Deformation of rotor blade

Fig. 2.12 Deformation of cross section



- (iii) rotor blade is a long slender beam and hence the uniaxial stress assumptions can be made; $\sigma_{\eta\eta} = 0$, $\sigma_{\zeta\zeta} = 0$ and $\tau_{\eta\zeta} = 0$.

The strain displacement field (accurate up to second order and accounting for moderate deflections) is defined as

$$\begin{aligned} \epsilon_{xx} = & u' + \frac{v'}{2} + \frac{w'^2}{2} - \lambda_T \phi'' + (\eta^2 + \zeta^2)(\theta_0 \phi' + (\phi')^2/2) \\ & - v''[\eta \cos(\theta_0 + \hat{\phi}) - \zeta \sin(\theta_0 + \hat{\phi})] \\ & - w''[\eta \sin(\theta_0 + \hat{\phi}) + \zeta \cos(\theta_0 + \hat{\phi})], \end{aligned} \quad (2.12)$$

$$\epsilon_{x\eta} = -(\zeta + \lambda_{T,\eta})\phi' = -\hat{\zeta}\phi', \quad (2.13)$$

$$\epsilon_{x\zeta} = (\eta - \lambda_{T,\zeta})\phi' = \hat{\eta}\phi'. \quad (2.14)$$

This results into equations being geometrically nonlinear. Here, v , w and $\hat{\phi}$ are axial, chord-wise bending, span-wise bending, and elastic twist, respectively; θ_0 is the blade pitch; η and ζ are the cross-sectional coordinates; and λ_T is the cross-sectional warping function. Also, $\hat{\phi}' = \phi' - w'v''$ and $u = u_e - \frac{1}{2} \int_0^x (v'^2 + w'^2) dx$.

Based on these assumptions and strain-displacement relationships (Eqs. 2.12–2.14), Hamilton's principle is used to derive the system of equations of motion. For a conservative system, it states that the true motion of a system, between prescribed initial conditions at time ψ_1 and final conditions at time ψ_2 , is that particular motion for which the time integral for the difference between potential and kinetic energies is a minimum. The generalized Hamilton's principle applicable to nonconservative systems is expressed as

$$\delta \Pi = \int_{\psi_1}^{\psi_2} (\delta U - \delta T - \delta W) d\psi = 0, \quad (2.15)$$

where δU , δT , and δW are virtual variations of strain energy, kinetic energy, and virtual work done by external force, respectively, and $\delta \Pi$ represents the total potential of the system.

The strain energy of the system can be written as follows:

$$U = \frac{1}{2} \int_0^R \int_A \int (\sigma_{xx} \epsilon_{xx} + \sigma_{x\eta} \epsilon_{x\eta} + \sigma_{x\zeta} \epsilon_{x\zeta}) d\eta d\zeta dx. \quad (2.16)$$

On addition of the smart layer, both the strain and kinetic energy of the existing structure are modified but the virtual work done due to applied forces remains unchanged. The kinetic and strain energy terms of the isotropic beam are defined in Appendix A. The nonlinear equations listed in Appendix A have been derived by Hodges and Dowell for elastic bending and torsion of twisted nonuniform rotor blades. Appendix B lists the section properties used in Appendix A. This theory was used by Epps and Chandra [11] to validate the rotating frequencies obtained by experiments. Also, Ganguli et al. [12] have correlated the analysis with vibration data and found that the analysis predicts vibration trends properly.

2.4.2 Smart Structure Expressions

The use of piezoceramic actuators changes the strain energy of the rotor blade. In the framework of above-mentioned assumptions, the equations of motion for a rotor blade/beam with surface-bonded piezoceramic actuators are derived. This derivation is generic for axial, bending, and torsion actuation and could be used as per the requirement of the application. The equations are used in Chaps. 8–11 for the active twist rotor. On using the variation of strain energy in the Hamilton's principle, we get

$$\delta U = \frac{1}{2} \int_0^R \int_A \int (\sigma_{xx} \delta \epsilon_{xx} + \sigma_{x\eta} \delta \epsilon_{x\eta} + \sigma_{x\zeta} \delta \epsilon_{x\zeta}) d\eta d\zeta dx. \quad (2.17)$$

The induced strains due to the bonding of piezoelectric layer were discussed in Eq. 2.7 and now superposition of these two constitutive equations will yield the derivation of smart terms.

$$U = \frac{1}{2} \int_0^R \int_A \int \{ \sigma_{xx} (\epsilon_{xx} - \lambda_{11}) + \sigma_{x\eta} (\epsilon_{x\eta} - \lambda_{12}) + \sigma_{x\zeta} (\epsilon_{x\zeta} - \lambda_{31}) \} d\eta d\zeta dx. \quad (2.18)$$

Here, we utilize only λ_{11} and λ_{12} in the above equation. The required bending and axial actuation can be obtained from λ_{11} and shear/torsion actuation is achievable from λ_{12} .

$$\begin{aligned} \text{where } \delta \epsilon_{xx} = & \delta u' + v' \delta v' + w' \delta w' + (\eta^2 + \zeta^2)(\theta_0' + \phi') \delta \phi' - \lambda_T \delta \phi'' \\ & - [\eta \cos(\theta_0 + \hat{\phi}) - \zeta \sin(\theta_0 + \hat{\phi})](\delta v'' + w'' \delta \hat{\phi}) \\ & - [\eta \sin(\theta_0 + \hat{\phi}) + \zeta \cos(\theta_0 + \hat{\phi})](\delta w'' - v'' \delta \hat{\phi}), \end{aligned} \quad (2.19)$$

$$\delta \epsilon_{x\eta} = -\hat{\zeta} \delta \phi', \quad (2.20)$$

$$\delta \epsilon_{x\zeta} = \hat{\eta} \delta \phi', \quad (2.21)$$

where $\hat{\zeta} = \zeta + \frac{\partial \lambda_T}{\partial \eta}$ and $\hat{\eta} = \eta - \frac{\partial \lambda_T}{\partial \zeta}$.

Performing the variation in strains and then nondimensionalizing with respect to ‘ R ’ (Radius of rotor), the following smart strain energy contributions are obtained:

$$U_{u'e} = \frac{1}{2} \int_0^1 A_0 dx, \quad (2.22)$$

$$U_{\hat{\phi}'} = \frac{1}{2} \int_0^1 \{A_1 (\theta_0' + \hat{\phi}' + w' v'') - A_4\} dx, \quad (2.23)$$

$$U_{v''} = \frac{1}{2} \int_0^1 \{-A_2(\cos \theta_0 - \hat{\phi} \sin \theta_0) + A_3(\sin \theta_0 + \hat{\phi} \cos \theta_0) + A_4 w'\} dx,$$

$$U_{\hat{\phi}''} = \frac{1}{2} \int_0^1 -A_5 dx, \quad (2.24)$$

$$U_{\hat{\phi}} = \frac{1}{2} \int_0^1 \{[A_2(\sin \theta_0 + \hat{\phi} \cos \theta_0) + A_3(\cos \theta_0 - \hat{\phi} \sin \theta_0)] v'' + [-A_2(\cos \theta_0 - \hat{\phi} \sin \theta_0) + A_3(\sin \theta_0 + \hat{\phi} \cos \theta_0)] w''\} dx, \quad (2.25)$$

$$U_{w''} = \frac{1}{2} \int_0^1 [-A_2(\sin \theta_0 + \hat{\phi} \cos \theta_0) - A_3(\cos \theta_0 - \hat{\phi} \sin \theta_0)] dx. \quad (2.26)$$

Hence, evaluating and deriving the new terms which arise due to surface bonding of the smart layer with appropriate substitution by section integrals yields

$$\begin{aligned} \frac{\delta U_{smart}}{m_0 \Omega^2 R^3} = & \int_0^1 [A_0 (\delta u_e') + A_1 (\theta_0' + \phi') \delta \phi' \\ & + (-A_2 \cos(\theta_0 + \hat{\phi}) + A_3 \sin(\theta_0 + \hat{\phi})) (\delta v'' + w'' \delta \hat{\phi}) \\ & + (-A_2 \sin(\theta_0 + \hat{\phi}) - A_3 \cos(\theta_0 + \hat{\phi})) (\delta w'' - v'' \delta \hat{\phi}) \\ & - (A_4 \delta \phi') - (A_5 \delta \hat{\phi}'')] dx, \end{aligned} \quad (2.27)$$

where A_0, A_1, A_2, A_3, A_4 and A_5 are the section properties due to piezoceramic actuation and are defined in Appendix B. The above derivation is generic for a beam undergoing displacements (axial, transverse bending, inplane bending, and torsion); also, it is generalized for axial, bending, and torsional actuation. A_0 and A_1 contribute to axial actuation, A_3 to bending actuation, and A_4 to shear actuation.

2.4.3 Identification of Smart Terms

The governing equations derived in Eq. 2.27 and shown in Appendix A contain a very large number of terms and are complicated to understand as they are derived for a generic cross-sectional beam with pretwist. To explain the physical significance, a symmetric section is taken as an example with θ_0 and β_p assumed to be zero. This simulates a rotating beam. In this case, the equations become simpler and hence the following element stiffness, damping, and mass matrices are obtained. The linear and nonlinear element force vectors are also shown for the same case.

$$\mathbf{K} = \frac{1}{2} \begin{bmatrix} \int_0^1 EA H_u'^T H_u' ds & 0 & 0 & 0 \\ 0 & \int_0^1 EI_z H'^T H' ds + \int_0^1 F_A H'^T H' ds - \int_0^1 m H^T H ds & \int_0^1 A_4 H''^T H' ds & + \int_0^1 A_3 H''^T H_\phi' ds \\ 0 & \int_0^1 A_4 H''^T H' ds & \int_0^1 EI_y H'^T H' ds + \int_0^1 F_A H'^T H' ds & 0 \\ 0 & - \int_0^1 A_3 H''^T H_\phi' ds & 0 & \int_0^1 m(k_m^2 - k_{m1}^2) H_\phi'^T H_\phi' ds + \int_0^1 GJ H_\phi'^T H_\phi' ds + \int_0^1 A_1 H_\phi'^T H_\phi' ds \end{bmatrix}, \quad (2.28)$$

$$\mathbf{C} = \frac{1}{2} \begin{bmatrix} 0 & - \int_0^1 2m H_u^T H_u ds & 0 & 0 \\ \int_0^1 2m H_u^T H_u ds & 0 & 0 & 0 \\ 0 & 0 & 0 & 0 \\ 0 & 0 & 0 & 0 \end{bmatrix}, \quad (2.29)$$

$$\mathbf{M} = \frac{1}{2} \begin{bmatrix} \int_0^1 m H_u^T H_u ds & 0 & 0 & 0 \\ 0 & \int_0^1 m H^T H ds & 0 & 0 \\ 0 & 0 & \int_0^1 m H^T H ds & 0 \\ 0 & 0 & 0 & \int_0^1 m k_m^2 H_\phi^T H_\phi ds \end{bmatrix}, \quad (2.30)$$

$$\mathbf{F}_L = \frac{1}{2} \begin{bmatrix} \int_0^1 m x H_u^T ds + \int_0^1 A_0 H_u^T ds \\ 0 \\ - \int_0^1 A_3 H''^T ds \\ + \int_0^1 A_4 H_\phi'^T \end{bmatrix}, \quad (2.31)$$

$$\mathbf{F}_{NL} = \frac{1}{2} \begin{bmatrix} -\int_0^1 E A k_A^2 \frac{\hat{\phi}^2}{2} H_u'^T ds \\ -\int_0^1 G J \hat{\phi}' w' H''^T ds - \int_0^1 (E I_z - E I_y) w'' \hat{\phi} H''^T ds \\ + \int_0^1 A_1 (\hat{\phi} w' + w'^2 v'') H''^T ds + \int_0^1 2m [\int_0^x (v' \dot{v}' + w' \dot{w}') d\xi] H^T ds \\ -\int_0^1 (2v' \int_x^1 m \dot{v} d\xi) H^T ds \\ -\int_0^1 G J \hat{\phi}' v'' H''^T ds - \int_0^1 (2w' \int_x^1 m \dot{w} d\xi) H^T ds \\ -\int_0^1 (E I_z - E I_y) v'' w'' \hat{\phi} H''^T ds \\ -\int_0^1 (E A k_A^2 \hat{\phi}' u_e' + G J w' v'') H_{\hat{\phi}}'^T ds \\ + \int_0^1 A_1 w' v'' H_{\hat{\phi}}'^T ds + \int_0^1 A_3 w'' \hat{\phi} H_{\hat{\phi}}'^T ds \end{bmatrix}. \quad (2.32)$$

The first, second, third, and fourth row and column in the matrix \mathbf{K} and rows in \mathbf{F} represent the axial, lag, flap, and torsion displacements. The off-diagonal terms in \mathbf{K} introduce couplings between the displacements. Depending on the type of actuation given, the smart terms get activated. For a symmetric section, A_0 and A_1 get activated in extension actuation, A_3 in bending actuation, and A_4 in torsion actuation. It should be noted that A_2 and A_5 are zero for a symmetric section. For bending actuation (A_3), lag bending–torsion and flap bending–torsion couplings are introduced through the stiffness matrix. Linear forcing is introduced into flap and lag bending equations and nonlinear forcing in the torsion equation. For torsion actuation (A_4), lag–flap bending coupling is introduced through the stiffness matrix and a linear forcing in the torsion equation.

Here, $F_A(x) = \int_1^x m x \, d\xi$ is the centrifugal axial force due to rotation. We observe that smart actuation terms cause inplane bending–transverse bending coupling and inplane bending–torsion coupling through the stiffness terms. The mass matrix does not contain any specific smart structure terms. The damping matrix shows the presence of the antisymmetric Coriolis effect, but no influence of smart terms. The linear force vector shows the influence of smart actuation on the axial, transverse bending, and torsion directions. Nonlinear smart terms are present in the force vector for inplane bending and torsion forces. The above equations of motion can be used to identify terms that can be tailored by designing a beam cross section to maximize the smart actuation effect and minimize the centrifugal stiffening effect.

2.4.4 Finite Element—Spatial Discretization

Each of the N beam elements has fifteen degrees of freedom as shown in Fig. 2.13. These degrees of freedom are distributed over five element nodes (2 boundary nodes and 3 interior nodes). There are six degrees of freedom at each element boundary node. These six degrees of freedom correspond to u , v , v' , w , w' , and $\hat{\phi}$. There are two internal nodes for axial deflection u and one internal node for elastic twist $\hat{\phi}$. Between elements, there is continuity of displacements and slope for flap and lag bending deflections, and continuity of displacement for elastic twist and axial deflections. These elements ensure physically consistent linear variations of bending

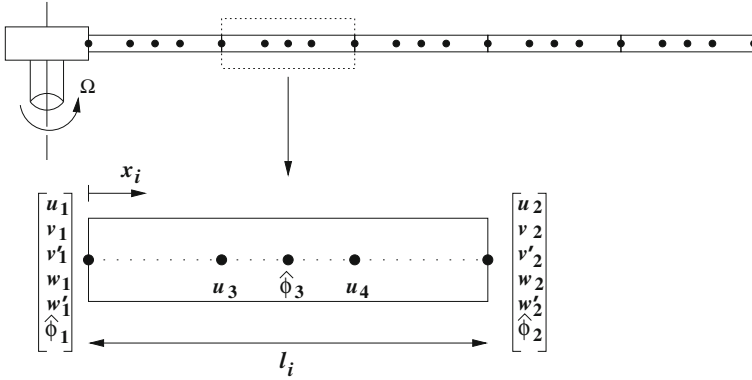


Fig. 2.13 The 15-DOF finite element used for spatial discretization of rotor blade

moments and torsional moment, and quadratic variation of axial force within each element. Using the interpolating polynomials, the distribution of deflections over a beam element is expressed in terms of the elemental nodal displacements \mathbf{q}_i . The shape functions used are Hermite polynomials for lag and flap bending, and Lagrange polynomials for axial and torsion deflection. For the i th beam element, the elemental nodal displacement vector is defined as

$$\mathbf{q}_i^T = [u_1, u_2, u_3, u_4, v_1, v'_1, v_2, v'_2, w_1, w'_1, w_2, w'_2, \hat{\phi}_1, \hat{\phi}_2, \hat{\phi}_3]. \quad (2.33)$$

Assembling the blade finite element equations and applying boundary conditions results in Eq. (2.16) becoming,

$$\mathbf{M}\ddot{\mathbf{q}}(\psi) + \mathbf{C}\dot{\mathbf{q}}(\psi) + \mathbf{K}\mathbf{q}(\psi) = \mathbf{F}(\mathbf{q}, \dot{\mathbf{q}}, \psi). \quad (2.34)$$

The nodal displacement vector \mathbf{q} is a function of time and all nonlinear terms have been moved into the force vector on the right-hand side. The spatial functionality has been removed using finite element discretization and partial differential equations have been converted into ordinary differential equations.

2.4.5 Normal Mode Transformation

The finite element equations representing each rotor blade are transformed to normal mode space for efficient solution of blade response using modal expansion. Typically, 6–10 modes are used. The displacements are expressed in terms of normal modes as

$$\mathbf{q} = \Phi \mathbf{p}. \quad (2.35)$$

Substituting Eq. 2.35 into Eq. 2.34 leads to the normal mode equations of the following form:

$$\bar{\mathbf{M}}\ddot{\mathbf{p}}(\psi) + \bar{\mathbf{C}}\dot{\mathbf{p}}(\psi) + \bar{\mathbf{K}}\mathbf{p}(\psi) = \bar{\mathbf{F}}(\mathbf{p}, \dot{\mathbf{p}}, \psi). \quad (2.36)$$

These equations are nonlinear ODEs but their dimensions are much reduced compared to the full finite element Eq. 2.34. The normal mode mass, stiffness and damping matrix, and force vectors are defined as

$$\bar{\mathbf{M}} = \Phi^T \mathbf{M} \Phi, \quad \bar{\mathbf{C}} = \Phi^T \mathbf{C} \Phi, \quad \bar{\mathbf{K}} = \Phi^T \mathbf{K} \Phi, \quad \bar{\mathbf{F}} = \Phi^T \mathbf{F}. \quad (2.37)$$

The mode shapes or eigen vectors in Eqs. 2.35 and 2.37 are obtained by solving the general eigenvalue problem:

$$\mathbf{K}_s \Phi = \omega^2 \mathbf{M}_s \Phi. \quad (2.38)$$

Here, ω are the natural frequencies of the rotating blade.

2.4.6 Finite Element—Temporal Discretization

The blade normal mode Eq. 2.36 can be written in the following variational form:

$$\int_0^{2\pi} \delta \mathbf{p}^T \left(\bar{\mathbf{M}}\ddot{\mathbf{p}}(\psi) + \bar{\mathbf{C}}\dot{\mathbf{p}}(\psi) + \bar{\mathbf{K}}\mathbf{p}(\psi) - \bar{\mathbf{F}}(\mathbf{p}, \dot{\mathbf{p}}, \psi) \right) d\psi = 0. \quad (2.39)$$

Integrating Eq. 2.39 by parts, we obtain

$$\int_0^{2\pi} \begin{Bmatrix} \delta \mathbf{p} \\ \delta \dot{\mathbf{p}} \end{Bmatrix}^T \begin{Bmatrix} \bar{\mathbf{F}} - \bar{\mathbf{C}}\dot{\mathbf{p}} - \bar{\mathbf{K}}\mathbf{p} \\ \bar{\mathbf{M}}\dot{\mathbf{p}} \end{Bmatrix} d\psi = \begin{Bmatrix} \delta \mathbf{p} \\ \delta \dot{\mathbf{p}} \end{Bmatrix}^T \begin{Bmatrix} \bar{\mathbf{M}}\dot{\mathbf{p}} \\ 0 \end{Bmatrix} \Big|_0^{2\pi}. \quad (2.40)$$

Since the helicopter rotor is a periodic system with a time period of one revolution, we have $\dot{\mathbf{p}}(0) = \dot{\mathbf{p}}(2\pi)$. Imposing periodic boundary conditions on Eq. 2.40 results in the right-hand side becoming zero and yields the following system of first-order ordinary differential equations:

$$\int_0^{2\pi} \delta \mathbf{y}^T \mathbf{Q} d\psi = 0, \quad (2.41)$$

where

$$\mathbf{y} = \begin{Bmatrix} \mathbf{p} \\ \dot{\mathbf{p}} \end{Bmatrix}, \quad \mathbf{Q} = \begin{Bmatrix} \bar{\mathbf{F}} - \bar{\mathbf{C}}\dot{\mathbf{p}} - \bar{\mathbf{K}}\mathbf{p} \\ \bar{\mathbf{M}}\dot{\mathbf{p}} \end{Bmatrix}.$$

The nonlinear, periodic, ordinary differential equations are then solved for blade steady response using the finite element in time in conjunction with Newton–Raphson method [13]. Discretizing Eq. 2.41 over N_t time elements around the rotor disk (where $\psi_1 = 0$, $\psi_{N_t+1} = 2\pi$) and taking first-order Taylor series expansion about the steady-state value $\mathbf{y}_0 = [\mathbf{p}_0^T \ \dot{\mathbf{p}}_0^T]^T$ yields the following algebraic equations.

$$\sum_{i=1}^{N_t} \int_{\psi_i}^{\psi_{i+1}} \delta \mathbf{y}_i^T \mathbf{Q}_i(\mathbf{y}_0 + \Delta \mathbf{y}) d\psi = \sum_{i=1}^{N_t} \int_{\psi_i}^{\psi_{i+1}} \delta \mathbf{y}_i^T [\mathbf{Q}_i(\mathbf{y}_0) + \mathbf{K}_{ti}(\mathbf{y}_0) \Delta \mathbf{y}] d\psi = 0, \quad (2.42)$$

where

$$\mathbf{K}_{ti} = \begin{bmatrix} \frac{\partial \bar{\mathbf{F}}}{\partial \mathbf{p}} - \bar{\mathbf{K}} & \frac{\partial \bar{\mathbf{F}}}{\partial \dot{\mathbf{p}}} - \bar{\mathbf{C}} \\ 0 & \bar{\mathbf{M}} \end{bmatrix}_i.$$

Here, \mathbf{K}_{ti} is the tangential stiffness matrix for time element i and \mathbf{Q}_i is the load vector. Behavior of the modal displacement vector can be approximated in terms of shape functions and a vector of temporal nodal coordinates as follows:

$$\mathbf{p}_i(\psi) = \mathbf{H}(s) \mathbf{r}_i, \quad (2.43)$$

where $\mathbf{H}(s)$ are time shape functions (in terms of the element coordinate s) used for approximating the normal mode coordinate \mathbf{p} . Here \mathbf{r} is the temporal nodal coordinate. In this book, mixed Lagrange–Hermite polynomials are used for interpolation within the time element [14]. Substituting Eq. 2.43 and its derivative into Eq. 2.42 yields the time discretized blade response.

$$\mathbf{Q}^G + \mathbf{K}_t^G \Delta \mathbf{r}^G = 0, \quad (2.44)$$

where

$$\begin{aligned} \mathbf{Q}^G &= \sum_{i=1}^{N_t} \int_{\psi_i}^{\psi_{i+1}} \mathbf{H}^T \mathbf{Q}_i d\psi, \\ \mathbf{K}_t^G &= \sum_{i=1}^{N_t} \int_{\psi_i}^{\psi_{i+1}} \mathbf{H}^T \begin{bmatrix} \frac{\partial \bar{\mathbf{F}}}{\partial \mathbf{p}} - \bar{\mathbf{K}} & \frac{\partial \bar{\mathbf{F}}}{\partial \dot{\mathbf{p}}} - \bar{\mathbf{C}} \\ 0 & \bar{\mathbf{M}} \end{bmatrix}_i d\psi, \\ \Delta \mathbf{r}^G &= \sum_{i=1}^{N_t} \Delta \mathbf{r}_i. \end{aligned}$$

Solving the above equations iteratively yields the blade steady response.

2.5 Aerodynamic Models

The aerodynamic environment of a helicopter rotor in forward flight is extremely complex involving transonic flow on advancing blades and reversed flow on retreating blades. The blade is also exposed to unsteady variations in angle of attack and free-stream velocity. Because of the complexity of the flow, accurate modeling of the unsteady flow field on the blade requires a sophisticated analysis. This section deals with aerodynamic loads due to blade/airfoil motion only. The aerodynamic loads enter the blade governing equations through their contribution to the external virtual work in Hamilton's principle.

The aerodynamic modeling of a rotor can be divided into two parts: a local blade element model and a global wake model. In this book, an unsteady aerodynamic model proposed by Leishman and Beddoes [15] is used to estimate the aerodynamic loads due to blade motion. The flow is assumed to be under a linear attached potential flow regime. Separated flow and dynamic stall effects are not modeled.

2.5.1 Attached Flow Formulation

The attached flow formulation is based on the work of Leishman and Beddoes [16]. This model implicitly includes the effects of compressibility. Also, this model requires few empirical constants which can be derived from static airfoil data. In this formulation, the unsteady lift, drag, and pitching moment are assumed to consist of circulatory and impulsive (noncirculatory) components. These airloads are calculated using an indicial response representation implemented in the form of a finite-difference discretization of integral equations. This method determines the aerodynamic loadings due to a step change in the downwash at the three-quarter chord position. The circulatory loads include the effects of the near shed wake. The impulsive loads are due to the presence of propagating pressure waves.

2.5.2 Reverse Flow

In forward flight, an inboard region of the retreating side of the rotor disk experiences reverse flow. In this reverse flow region, the forward speed component of the total velocity relative to the blade becomes larger than the velocity component due to the rotational speed. Therefore, the velocity relative to the blade is directed from the trailing edge to the leading edge. If the blade dynamics are neglected, the reverse flow region is given by Eq. 2.45, which represents a circular region (Fig. 2.14).

$$r \leq -\mu \sin\psi. \quad (2.45)$$

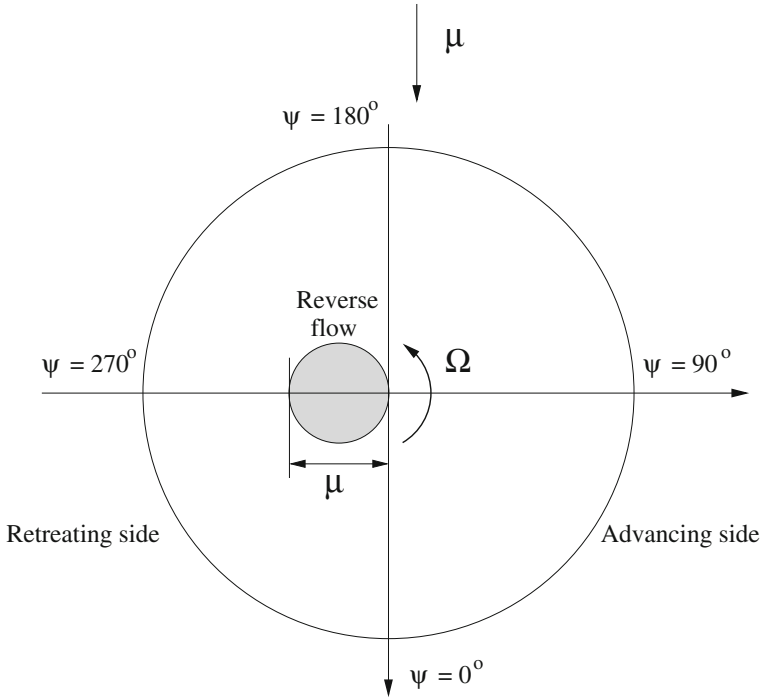


Fig. 2.14 Reverse flow region

The reverse flow boundary is thus a circle of diameter μ , centered at $r = \mu/2$ for the azimuth station of 270° on the retreating side. Reverse flow causes the aerodynamic center of the airfoil to shift from x_{ac} to $(c - x_{ac})$, where x_{ac} is the aerodynamic center of the airfoil.

2.5.3 Inflow and Rotor Wake Modeling

The wake behind the rotor disk determines the induced inflow distribution over the disk and plays a very important role in the prediction of blade response, vibration, and rotor performance. An accurate modeling of the induced inflow is essential, especially at low-speed flight condition. At low speed, the wake stays close to the disk and has a dominating influence on blade airloads. There are many wake models available with varying levels of complexity and accuracy. Two inflow models are used. One is the simple linear inflow model and the other is the elaborate free wake model.

Linear Inflow Model

In a linear inflow model, the induced velocities are assumed to vary linearly across the rotor disk:

$$\lambda = \mu \tan \alpha_s + \lambda_i = \mu \tan \alpha_s + \frac{C_T/2}{\sqrt{\lambda^2 + \mu^2}} (1 + \kappa_x x \cos \psi + \kappa_y x \sin \psi), \quad (2.46)$$

where λ is the total inflow ratio, λ_i is the induced inflow ratio, and α_s is the forward tilt of the rotor disk plane. There are many forms of this model available in literature. One form is called Drees [17] model, where κ_x and κ_y are defined as

$$\begin{aligned} \kappa_x &= \frac{4}{3} \left[(1 - 1.8\mu^2) \sqrt{1 + \left(\frac{\lambda}{\mu}\right)^2} - \frac{\lambda}{\mu} \right], \\ \kappa_y &= -2\mu. \end{aligned} \quad (2.47)$$

This simple inflow model captures the global effects of rotor wake and is usually satisfactory for high-speed flight condition, more so for rotor performance and stability predictions. However, this model becomes much less accurate at low-speed flight or hover condition when the inflow distribution becomes highly nonuniform over the rotor disk. The linear inflow model can be easily implemented in rotor aeroelastic analysis due to its simplicity.

Free Wake Model

The free wake model used was developed by Bagai and Leishman [17]. The wake is divided into three distinct regions: near wake, rolling-up wake, and far wake. The near wake is of prime importance to its generating blade due to its proximity. The most difficult part of the wake analysis is to calculate the wake geometry. In the present wake model, the wake is modeled as a finite number of vortex filaments, which are trailed and shed into the wake. These filaments are convected with the local flow velocity, which consists of the free-stream velocity and the wake self-induced velocity. Since the self-induced velocity is, in turn, a function of the wake geometry, the analysis is highly nonlinear in nature. A rigid wake geometry, which consists of a simple helix convected by the free stream and the mean inflow, is used to initialize the calculation, and then the wake geometry evolves until it is stabilized. The vorticity strength is determined by the bound circulation which in turn is calculated from the lift distribution along the rotor blade. Once the vorticity strength and wake geometry are known, the induced velocity can be evaluated using the Biot–Savart law. Free wake models can capture nonuniform inflow distributions expected at low forward speeds but at the cost of much greater computational effort compared to linear inflow models.

2.5.4 Dynamic Stall Formulation

This is characterized by separation at the leading edge and the shedding of concentrated vorticity from the leading edge region. The vorticity is swept downstream chord-wise and significantly affects the load distribution on the airfoil. The vortex convection rate is calculated using a nondimensional time parameter based on the distance traveled by the airfoil in terms of semi-chord length. By monitoring the excess lift and the center of pressure movement, the vortex-induced pitching moment is computed. As the vortex reaches the trailing edge, the model assumes rapid decay of the increment lift.

Inflow distribution over the rotor disk can be computed using either a simple uniform linear inflow model or a free wake model. Typically, the actual wake of a rotor is quite nonuniform and requires a free wake model for accurate vibratory load predictions.

2.6 Blade and Hub Loads

Once the blade steady-state response is obtained, the loads acting at any section of the blade are calculated by summation of the aerodynamic and inertial loads. The blade root loads are given by

$$\begin{Bmatrix} F_{xR} \\ F_{yR} \\ F_{zR} \\ M_{xR} \\ M_{yR} \\ M_{zR} \end{Bmatrix} = \int_0^R \begin{Bmatrix} L_u \\ L_v \\ L_w \\ -L_v w + L_w v + M_u \\ L_u w - L_w(x + u) + M_v \\ -L_u v + L_v(x + u) + M_w \end{Bmatrix} dx. \quad (2.48)$$

Here, L_u , L_v , and L_w are the forces acting on element dx along the x , y , and z directions and M_u , M_v , and M_w are the moments along the x , y , and z directions, respectively. The section loads are in the rotating frame and are directed toward the undeformed blade axes. In the fixed frame, the rotor hub loads can be expressed as

$$\begin{aligned} F_X^H(\psi) &= \sum_{m=1}^{N_b} (F_x^m \cos\psi_m - F_y^m \sin\psi_m - F_z^m \cos\psi_m \beta_p), \\ F_Y^H(\psi) &= \sum_{m=1}^{N_b} (F_x^m \sin\psi_m + F_y^m \cos\psi_m - F_z^m \sin\psi_m \beta_p), \\ F_Z^H(\psi) &= \sum_{m=1}^{N_b} (F_x^m \beta_p + F_z^m), \end{aligned} \quad (2.49)$$

$$\begin{aligned}
M_X^H(\psi) &= \sum_{m=1}^{N_b} (M_x^m \cos \psi_m - M_y^m \sin \psi_m - M_z^m \cos \psi_m \beta_p), \\
M_Y^H(\psi) &= \sum_{m=1}^{N_b} (M_x^m \sin \psi_m + M_y^m \cos \psi_m - M_z^m \sin \psi_m \beta_p), \\
M_Z^H(\psi) &= \sum_{m=1}^{N_b} (M_x^m \beta_p + M_z^m).
\end{aligned}$$

The hub loads are expanded in a Fourier series and the steady and harmonic components are calculated. The steady hub loads are required to calculate the steady rotor forces which are in turn utilized for trim equilibrium equations to obtain the trim controls. After trim controls have been calculated, the blade response for the current trim solution is calculated using an iterative process. For a N_b -bladed rotor, the fixed frame hub loads contain only steady and integer multiples of N_b/rev harmonics. In general, the N_b/rev harmonics are the dominant vibratory components. The analysis of hub loads is needed for both trim and vibration predictions.

2.6.1 Coupled Trim

Once the hub loads are obtained, the helicopter needs to be trimmed. Trim is defined as the condition where the steady forces and moments acting on the helicopter sum to zero and simulate the condition for steady level flight. The trim solution for the helicopter involves finding the pilot control angles θ at which the six steady forces and moments acting on the helicopter are zeros:

$$\mathbf{F}(\theta) = \mathbf{0}, \quad (2.50)$$

where

$$\mathbf{F}^T = [F_1, F_2, F_3, F_4, F_5, F_6]. \quad (2.51)$$

The following equations are derived from the force equilibrium of a helicopter in steady level flight.

$$\begin{aligned}
F_1 &= D_F \cos \theta_{FP} + H \cos \alpha_s - T \sin \alpha_s, \\
F_2 &= Y_F + Y \cos \phi_s + T \sin \phi_s + T_{tr}, \\
F_3 &= T \cos \alpha_s \cos \phi_s - D_F \sin \theta_{FP} + H \sin \alpha_s - Y \sin \phi_s - W - L_{ht}, \\
F_4 &= M_{xR} + M_{xF} + Y_F (\bar{h} \cos \phi_s + y_{cg} \sin \phi_s) + W (\bar{h} \sin \phi_s - y_{cg} \cos \phi_s) + T_{tr} (\bar{h} - z_{tr}), \\
F_5 &= M_{yR} + M_{yF} + W (\bar{h} \sin \alpha_s - x_{cg} \cos \alpha_s) - D_F (h \cos(\alpha_s + \theta_{FP}) \\
&\quad + x_{cg} \sin(\alpha_s + \theta_{FP})) + L_{ht} (x_{ht} - x_{cg}), \\
F_6 &= M_{zR} + M_{zF} + T_{tr} (x_{tr} - x_{cg}) - D_F Y_{cg} \cos \alpha_s - Y x_{cg} \cos \phi_s,
\end{aligned} \quad (2.52)$$

where F_1 , F_2 , and F_3 are, respectively, the vehicle force equilibrium residuals in the X , Y , and Z directions in the fuselage axes; and F_4 , F_5 , and F_6 are the vehicle rolling, pitching, and yawing moment equilibrium residuals about the vehicle cg, respectively. Also, H , Y , and T are, respectively, rotor drag, side force, and thrust; and D_F , Y_F , and W are, respectively, fuselage drag, side force, and gross weight. The terms T_{tr} , x_{tr} , and z_{tr} denote the tail rotor thrust, the distance of the tail rotor hub behind the vehicle cg, and the distance of the tail rotor hub above the vehicle cg. The horizontal tail is located at a distance x_{ht} behind the vehicle cg. The terms in the three moment, M_{xR} and M_{xF} , denote the rotor and fuselage moments, respectively. The forces act on the rotor hub and the moments act about the rotor hub. In addition, x_{cg} and y_{cg} and h are, respectively, the relative location of the rotor hub center with respect to the vehicle center of gravity in the X_F , Y_F , and Z_F directions; α_s (positive for forward flight) and ϕ_s (positive advancing down) are the longitudinal and lateral shaft tilts, respectively, and θ_{FP} is the flight path angle relative to an axis perpendicular to the gravity vector.

The forces acting on the fuselage are calculated using

$$\begin{aligned}
 D_F &= \frac{\gamma N_b}{6a\sigma} \frac{f}{A} \mu^2, \\
 Y_F &= \frac{\gamma N_b}{6a\sigma} C_{yF} \mu^2, \\
 M_{xF} &= \frac{\gamma N_b}{6a\sigma} C_{mxF} \mu^2, \\
 M_{yF} &= \frac{\gamma N_b}{6a\sigma} C_{myF} \mu^2, \\
 M_{zF} &= \frac{\gamma N_b}{6a\sigma} C_{mzF} \mu^2, \\
 W &= \frac{\gamma N_b}{3a\sigma} (C_W - C_{lF} \mu^2 / 2) \mu^2,
 \end{aligned} \tag{2.53}$$

where γ is the lock number, N_b is the number of blades, a is the reference lift curve slope, σ is the solidity, f/A is the fuselage flat plate area, C_{yF} is the fuselage side force coefficient, C_{mxF} is the fuselage yawing moment coefficient, C_W is the helicopter weight coefficient, and C_{lF} is the lift coefficient.

For propulsive trim, the unknown quantities to be determined from the equilibrium equations are

$$\theta^T = [\alpha_s, \phi_s, \theta_0, \theta_{1c}, \theta_{1s}, \theta_{tail}], \tag{2.54}$$

where the rotor trim parameters θ_0 , θ_{1c} , and θ_{1s} govern the main rotor blade.

The trim equations are solved iteratively using a Newton–Raphson procedure. A coupled trim procedure is carried out to solve the blade response, pilot input trim controls, and vehicle orientation, simultaneously. This procedure is called coupled trim since the blade response Eq. 2.44 and trim Eq. 2.50 are simultaneously solved thereby accounting for the influence of elastic blade deflections on the rotor steady forces:

$$\Delta\theta_i = - \left[\frac{\partial \mathbf{F}}{\partial \theta} \right]_{\theta=\theta_0}^{-1} \mathbf{F}(\theta_i). \quad (2.55)$$

For a converged solution, the $\Delta\theta$ and F are zero. The controls are updated as follows:

$$\theta_{i+1} = \theta_i + \Delta\theta_i. \quad (2.56)$$

The trim Jacobian, $[\partial F/\partial\theta]$, is calculated using a forward finite-difference approximation at $\theta = \theta_0$, and it is generally held constant throughout the analysis to save computational time.

The coupled trim is solved iteratively until convergence. The coupled trim procedure is essential for elastically coupled blades since elastic deflections play an important role in the net steady forces and moments generated by the rotor.

2.7 Organization of Aeroelastic Analysis

Figure 2.15 shows the flow of the aeroelastic formulation and analysis which was discussed in previous sections. Starting with the input to the analysis, structural modeling is carried out as the first step. The governing differential equations thus obtained are space and time dependent. These equations are nonlinear and periodic in nature. These equations are discretized using FEM (Finite element method) in space and rotating blade natural frequencies and mode shapes are found. Normal mode transformation is done to reduce the number of degrees of freedom and thus reduce the computational time. Aerodynamic modeling is the next major step. Here, the type of aerodynamic model is decided and the governing equations are discretized in time. Thus, both space and time dependencies are removed, resulting into nonlinear, algebraic equations which are solved using the Newton–Raphson method. Blade loads and the helicopter steady loads are calculated which are in turn required for performing trim calculations. Blade steady-state response, vehicle orientation, and trim control angles are solved for iteratively using a coupled trim procedure.

2.8 Summary

The baseline aeroelastic analysis for a helicopter rotor is discussed in this chapter along with the basic physics of piezoelectric materials. The approaches for determining the blade response, blade and hub loads, and vehicle trim are highlighted. The influence of piezoelectric material on the smart rotor equations is highlighted. These equations are used for the active twist rotor. For the active flap rotor, the ‘non-smart’ equations will be used and the piezoelectric actuator is addressed separately.

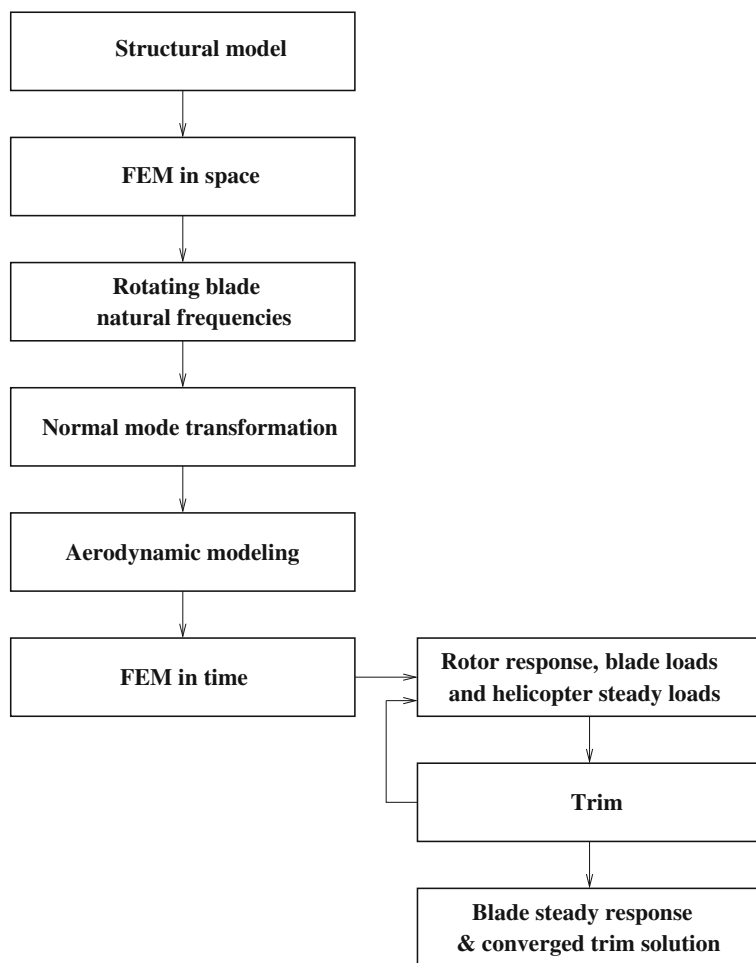


Fig. 2.15 Organization of aeroelastic analysis

References

1. Durr, J., Schmidt, U., Zaglauer, W.: On the integration of piezoceramic actuators in composite structures for aerospace applications. *J. Intell. Mater. Syst. Struct.* **10**, 880–889 (1999)
2. Srinivasan, A., McFarland, M.: *Smart Structures: Analysis and Design*. Cambridge University Press, Cambridge (2000)
3. Crawley, E.: Intelligent structures for aerospace: a technology overview and assessment. *J. Am. Inst. Aeronaut. Astronaut.* **32**(8), 1689–1699 (1994)
4. Loewy, R.: Recent developments in smart structures with aeronautical applications. *Smart Mater. Struct.* **6**(5), 11–42 (1997)
5. Park, S., Shrout, T.: Relaxor based ferroelectric single crystals for electromechanical actuators. *Mater. Res. Innov.* **1**, 20–25 (1997)

6. Liu, S., Ren, W., Mukherjee, B.: The piezoelectric shear strain coefficient of $\langle 111 \rangle$ piezocrystals. *Appl. Phys. Lett.* **83**(14), 2886–2888 (2003)
7. Crawley, E., Anderson, E.: Detailed models of piezoceramic actuation of beams. In: *Proceedings of the 30th AIAA/ASME/ASCH/AHS/ASC Structures, Structural Dynamics Conference*, Washington, DC (1989)
8. Hong, C., Chopra, I.: Modeling and validation of induced strain actuation of composite coupled plates. *J. Am. Inst. Aeronaut. Astronaut.* **37**(3), 372–377 (1999)
9. Chen, W., Saleeb, A.: *Constitutive Equations for Engineering Materials: Elasticity and Modeling*, vol. 1. Wiley-Interscience, New York (1952)
10. Hodges, D., Dowell, E.: Non-linear equations of motion for the elastic bending and torsion of twisted nonuniform rotor blades. Technical report NASA TN D-7818 (1974)
11. Epps, J., Chandra, R.: The natural frequencies of rotating composite beams with tip sweep. *J. Am. Helicopter Soc.* **41**, 29–36 (1996)
12. Ganguli, R., Chopra, I., Weller, W.: Comparison of calculated vibratory rotor hub loads with experimental data. *J. Am. Helicopter Soc.* **43**, 312–318 (1998)
13. Chopra, I., Sivaneri, T.: Aeroelastic stability of rotor blades using finite element analysis. Technical report NASA CR 166389 (1982)
14. Leishman, J.G., Beddoes, T.S.: A generalised model for airfoil unsteady aerodynamic behaviour and dynamic stall using the indicial method. In: *Proceedings of the 42nd Annual Forum of the American Helicopter Society*, Washington, DC, June, pp. 243–265 (1986)
15. Leishman, J.G., Beddoes, T.S.: A semi-empirical model for dynamic stall. *J. Am. Helicopter Soc.* **34**(3), 3–17 (1989); Leishman, J.G.: *Principles of Helicopter Aerodynamics*. Cambridge University Press, New York (2000)
16. Drees, J.M.: A theory of air flow through rotors and its application to some helicopter problems. *J. Helicopter Assoc. G. B.* **3**(2), 79–104 (1949)
17. Bagai, A., Leishman, J.G.: Rotor free-wake modeling using a pseudo-implicit technique—including comparisons with experimental data. *J. Am. Helicopter Soc.* **40**(3), 29–41 (1995)

Smart Helicopter Rotors

Optimization and Piezoelectric Vibration Control

Ganguli, R.; Thakkar, D.; Viswamurthy, S.R.

2016, XIII, 257 p. 213 illus., Hardcover

ISBN: 978-3-319-24766-3